Nanoscale Advances

ROYAL SOCIETY OF CHEMISTRY

PAPER

View Article Online
View Journal | View Issue

Cite this: *Nanoscale Adv.*, 2024, **6**, 6317

Layered MOF supported on 2D delaminated MXene ($Mo_2Ti_2C_3$) nanosheets boosted water splitting†

Maida Murtaza,[a] Komal Farooq,[a] Waqas Ali Shah,[ab] Iftikhar Ahmad[a] and Amir Waseem *[a]

Metal organic frameworks (MOFs) have a porous structure, high surface area, and high charge transfer, and they have been regarded as model electrocatalysts. Optimization of the electrocatalytic activity of MOFs is challenging, and an effective strategy for this optimization is the construction of a well-defined interfacial bond bridge. In this work, an *in situ* approach of composite synthesis is reported for MOF ($CoNiNH_2BDC$) with MXenes ($Mo_2Ti_2C_3$), as the electrocatalytic properties of MOF can be greatly enhanced with the incorporation of the conductive material MXene. The prepared composite material was characterized thoroughly using XRD, XPS, FESEM, EDX, TEM, and BET. The synergistic effect of both components of this composite material resulted in enhanced conductivity and the number of active sites, which led to enhanced electrocatalytic performance. The $CoNiNH_2BDC$ MOF with different ratios of $Mo_2Ti_2C_3$ MXene were synthesized, and the resulting materials were evaluated for oxygen evolution reaction (OER) and hydrogen evolution reaction (HER) activities. It was observed that the MOFMX3 attained a 10 mA cm^{-2} current density at 1.44 V for OER and −0.037 V for HER (*vs.* RHE), and lower values of Tafel slopes of 44.8 mV dec^{-1} for OER and 45 mV dec^{-1} for HER in 0.1 M KOH were achieved. The higher double layer capacitance (C_{dl}) values lead to high electrochemical surface area (ECSA) values. Lower Tafel slope values for MOFMX3 show that the presence of MXene nanosheets in the hybrid provides support to the layered and porous configuration of MOF, and the chances of the interaction of electrolyte to the catalytically active sites are significantly enhanced. This work highlights the idea of growing bimetallic MOFs on $Mo_2Ti_2C_3$ MXene using an interdiffusion reaction strategy and opens up an avenue for designing highly electrocatalytic systems.

Received 29th July 2024
Accepted 5th October 2024

DOI: 10.1039/d4na00630e

rsc.li/nanoscale-advances

1. Introduction

Sustainable energy production is a goal around the globe, and as the population of the world increases, energy demands increase. Therefore, it is crucial to find energy sources that are environmentally friendly, sustainable and less hazardous to life on this planet.[1,2] Hydrogen is one of the most used energy sources, and hydrogen is mostly produced from the combustion of coal, which is harmful as it is the cause of global warming and increased carbon dioxide levels in the environment. Therefore, a safe source of hydrogen production is required that can suppress CO_2 emissions in the environment and make life on Earth more sustainable. Water splitting is one of the sustainable sources for the production of green hydrogen. Water splitting comprises water oxidation, *i.e.* oxygen evolution reaction (OER), occurring at the anode, and water reduction reaction, *i.e.* hydrogen evolution reaction (HER), occurring at the cathode.[3] To achieve better efficiency of these OER and HER reactions, we need electrocatalysts that are economical, abundant, and non-toxic and those can compensate for the sluggish reaction kinetics and provide results with lower overpotential values. An emerging class of compounds comprising inorganic metal and an organic ligand (also known as linker) is metal organic frameworks (MOFs) that possess high porosity, tunable structure, and high flexibility.[4–6] In the structure of MOFs, metal units are uniformly dispersed in the network; therefore, MOFs behave as efficient homogeneous and heterogeneous catalysts.[7–9] MOFs have been reported as electrocatalysts, but MOFs have poor conductivity, and it is required to develop MOF composites with conductive materials for enhancing the conductivity of MOFs; to date, a limited number of such MOF composites have been reported for their applications in electrocatalysis, and there is a room of research available to design and develop MOF composites for better efficient OER and HER catalysts.[10,11]

A class of 2D materials known as MXene is a highly conductive material synthesized from the MAX phase, commonly known for layered materials with a common formula

[a]*Department of Chemistry, Quaid-i-Azam University, Islamabad, Pakistan. E-mail: amir@qau.edu.pk*

[b]*School of Chemistry and Chemical Engineering, Henan Normal University, Xinxiang, 453007, China*

† Electronic supplementary information (ESI) available. See DOI: https://doi.org/10.1039/d4na00630e

$M_{n+1}AX_n$ ($n = 1, 2, 3$), where M represents metals (such as M = Ti, V, and Mo), A is usually aluminum/gallium and X denotes N/C. Some basic properties that MXenes offer are high conductivity, corrosion resistance, layered structure, and faster charge transfer mechanism[12–14] and can be modified in various ways to achieve desired properties[15] and MOF composites with conductive substrates, such as rGO and CNTs, have also been reported.[16] The combination of MXenes with MOFs can result in a better catalyst/electrocatalyst, but this combination is rarely reported.[15,17] With all of the above-mentioned discussion, we designed MOF@MXene hybrids as electrocatalysts for OER and HER activities. A 2D MOF was synthesized using an aminoterephthalic acid linker with cobalt and nickel, which was further decorated on $Mo_2Ti_2C_3$ MXene sheets by applying an interdiffusion reaction strategy. Detailed characterizations, such as XRD, FESEM, EDX, TEM, XPS, and BET, were carried out to confirm the composite synthesis. In view of the tunability in the structure of MOFs and their chemical diversity, the approach shown in this work, *i.e.*, *in situ* hybridization, is most favorable for the synthesis of MOF MXene hybrids for the synthesis of electrocatalysts for green hydrogen production.

2. Materials and methods

2.1 Materials

Molybdenum titanium aluminum carbide was purchased from Chemazone Inc., Nanochemazone™ (Canada). *N*,*N*-Dimethylformamide (DMF), potassium hydroxide (KOH), nickel nitrate hexahydrate ($Ni(NO_3)_2 \cdot 6H_2O$), and hydrogen fluoride (HF) were purchased from ISOLAB. Aminoterephthalic acid (NH_2BDC), cobalt nitrate hexahydrate ($Co(NO_3)_2 \cdot 6(H_2O)$), and glassy carbon electrode were bought from Sigma-Aldrich. All the chemicals were used without further purification.

2.2 Synthesis of $Mo_2Ti_2C_3T_x$

From the MAX phase ($Mo_2Ti_2AlC_3$), the 'A' layer was removed for the synthesis of $Mo_2Ti_2C_3$ MXene by etching with HF. In 30 ml of HF, 2 g of $Mo_2Ti_2AlC_3$ was added slowly, and the solution was kept at magnetic stirring for 24 hours at 40 °C. Centrifugation and washing of the solution were done at 8000 rpm with distilled water until the pH reached 7 (neutral). The material was dried overnight at 70 °C.

2.3 Synthesis of $CoNH_2BDC$, $NiNH_2BDC$, and $CoNiNH_2BDC$ MOF

$CoNiNH_2BDC$ was synthesized by the reported solvothermal process with slight amendments.[18] Concisely, 0.8 g of aminoterephthalic acid (NH_2BDC), 0.6 g of each nickel and cobalt salt were added into 40 ml of DMF and to homogenize this mixture, and it was kept at magnetic stirring for an hour. The homogenized mixture was then kept in the oven at a temperature of 140 °C for 24 hours after transferring into a Teflon-lined autoclave. After heating for 24 hours, the autoclaves were kept closed until they cooled at room temperature; then, the washing of the synthesized material was done with DMF and ethanol by centrifugation at 5000 rpm (three times), and the material was dried overnight at 70 °C.

$CoNH_2BDC$ was synthesized using the same above-mentioned solvothermal method. A mixture of 0.6 g of $Co(NO_3)_2 \cdot 6H_2O$, 0.4 g of NH_2BDC, and 40 ml of DMF was kept at magnetic stirring for an hour, then poured into the Teflon-lined autoclave and kept in the oven at 140 °C for 24 hours.

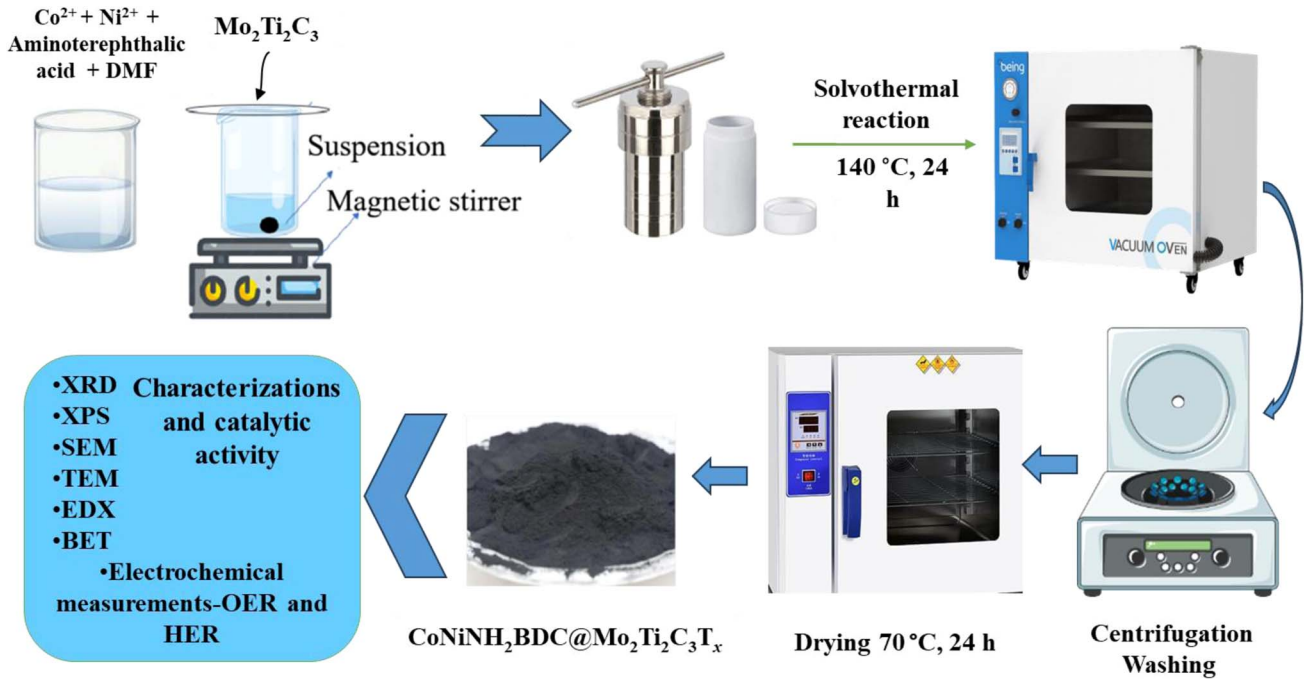

Scheme 1 Schematic diagram for the synthesis of $CoNiNH_2BDC@Mo_2Ti_2C_3T_x$.

Centrifugation, washing, and drying of the prepared material were performed under the same conditions mentioned above for the synthesis of $CoNiNH_2BDC$.

Synthesis of $NiNH_2BDC$ was done using a method similar to $CoNH_2BDC$ (0.6 g of $Ni(NO_3)_2 \cdot 6H_2O$), and 0.4 g of NH_2BDC was added to DMF (40 ml). The solvothermal reaction was carried out under similar temperature and time conditions, and similar conditions for centrifugation, washing, and drying.

2.4 Synthesis of $CoNiNH_2BDC$ MOF@$Mo_2Ti_2C_3T_x$

$CoNiNH_2BDC$@MXene hybrid was prepared analogous to that of the $CoNiNH_2BDC$ except for the addition of a definite quantity of etched MXene along with 0.6 g of $Ni(NO_3)_2 \cdot 6H_2O$, 0.6 g $Co(NO_3)_2 \cdot 6H_2O$, 0.8 g of NH_2BDC, and 40 ml of DMF. The mixture was kept at magnetic stirring for one hour for homogenization. The homogenized mixture was then transferred into a Teflon-lined autoclave and kept in the oven at a temperature of 140 °C for 24 hours. After heating for 24 hours, the autoclaves remained closed until they cooled at room temperature; then, the washing of the synthesized material was done by centrifugation at 500 rpm (three times) with DMF and ethanol subsequently, and the material was dried overnight at 70 °C. Preparation of $CoNiNH_2BDC$@$Mo_2Ti_2C_3T_x$ hybrids was prepared as described above; however, during MOF synthesis, different concentrations of $Mo_2Ti_2C_3T_x$ (5, 10, and 15 wt%) were added to the solution, and these prepared hybrids were named MOFMX1, MOFMX2 and MOFMX3, respectively, as described in Scheme 1.

2.5 Characterizations

X-ray diffraction analysis was performed using the "Bruker D2 Phaser" instrument with CuKα radiation ($\lambda = 1.54$ Å) source. Field emission scanning electron microscopy analyses were performed using a "Zeiss Ultra Plus" instrument equipped with EDX spectroscopy. The specific surface area of the synthesized material was calculated using "Quantachrome instruments NOVA Touch". For XPS measurements, a "Thermo K-alpha" system was used with a monochromatized AlKα X-ray source. A "JEOL JEM-2100F" field-emission transmission electron microscope was used to obtain the TEM images.

2.6 Electrochemical study

Using the Zahner Potentiostat with a three-electrode cell design, the electrocatalytic activity of the prepared catalysts was measured, and a 0.1 M KOH solution was used as an electrolyte. Catalyst-loaded glassy carbon electrode was used as the working electrode, and platinum wire and Ag/AgCl were used as counter and reference electrodes, respectively. The Nernst equation was used for converting potential to *versus* reversible hydrogen electrode (RHE):[19,20]

$$E_{RHE} = E_{Ag/AgCl} + 0.059\ pH + E^0_{Ag/AgCl},$$

where E_{RHE} is the applied potential *vs.* RHE; $E_{Ag/AgCl}$ is the applied potential *vs.* Ag/AgCl and E_0 (Ag/AgCl) is the standard Ag/AgCl electrode potential, which is 0.1976 V at 25 °C. In the potential ranging from 1.1 to 1.8 V *vs.* RHE at a scan rate of 1 mV s^{-1}, the linear sweep voltammetry (LSV) and cyclic voltammetry (CV) measurements were recorded.[21] At a fixed potential value of 1 V *vs.* RHE and in the frequency range of 0.1 Hz to 100 kHz, electrochemical impedance spectroscopy (EIS) measurement was performed for an estimation of charge transfer resistance. CV cycles in a non-faradaic potential range at different scan rates of 50–300 mV s^{-1} gave the value of electrical double-layer capacitance (C_{dl}). Calculation of the C_{dl} value was done by linear fitting of the plot, where the current density against different scan rates was plotted.[20] The working electrode was prepared by depositing the catalyst on a glassy carbon electrode (2 mm dia.). Catalyst ink was prepared by mixing 5 mg of the catalyst in 200 µl of ethanol, sonication was done for one hour and 10 µl of the prepared ink was drop cast on the glassy carbon electrode surface and dried for half an hour.

3. Results and discussion

3.1. Characterizations

The powder X-ray diffraction (XRD) pattern of the Max phase ($Mo_2Ti_2AlC_3$) (Fig. S1†) shows clear and distinct peaks. The Max phase ($Mo_2Ti_2AlC_3$) shows the diffraction peaks of interest at the 2θ values of 8.9° (002), 19.1° (004), and 28.5° (006). After etching the Max phase with HF, these diffraction peaks shifted to lower 2θ values of 6.58°, 12.65°, and 24.2° for plane indices of (002), (004), and (006), respectively, as reported previously.[22,23] The increase in the *d*-spacing ascribed to the intercalation of water molecules and surface termination groups ($Mo_2Ti_2C_3T_x$ MXene), *e.g.* T_x = –O, –OH, and –F, after the removal of the "Al" layer.[24] The appearance of a prominent peak at the (002) plane of $Mo_2Ti_2C_3$ MXene, which is more intense than the pristine

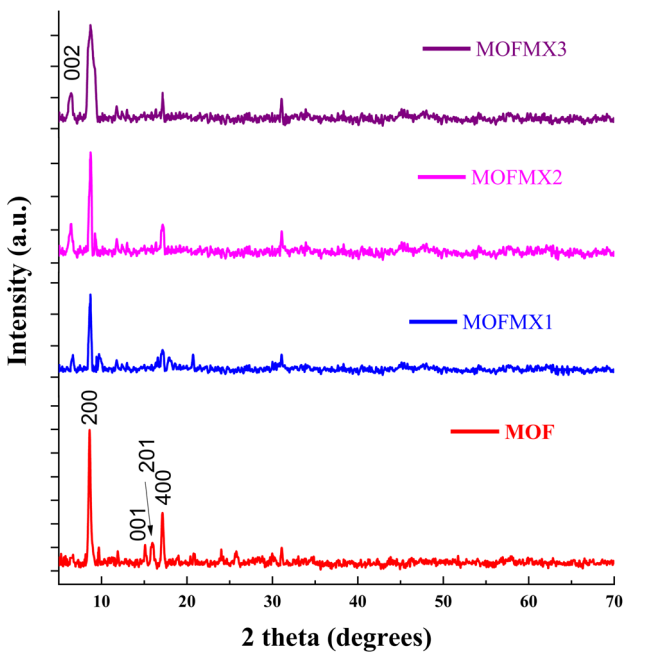

Fig. 1 XRD patterns of $CoNiNH_2BDC$ MOF and MOFMX composites.

Max phase, suggests structural stability and crystallinity (Fig. S1†) after delamination. The peaks between the 2θ values of 33°–45° and 50–70° almost disappeared after successful "Al" etching from the $Mo_2Ti_2AlC_3$ Max phase. The successful synthesis of MOFMX composites is shown in Fig. 1. The important signals appear at 2θ values of 8.6°, 14.6°, 15.1°, 16.1°, and 17.2° and can be assigned to (200), (00$\bar{1}$), (20$\bar{1}$), and (400) planes, respectively, of a layered triclinic structure. Similarly, the other signals are in the range of 2θ values of 25°–35°. In addition, Fig. S2† shows the XRD signals of $CoNH_2BDC$ MOF and $NiNH_2BDC$ MOF, and the overall XRD pattern of $CoNiNH_2BDC$ MOF agrees well with the XRD standard card of Ni-MOF (CCDC No. 985792), as previously reported.[18,25] *In situ* growth of MOF on the surface of layers of MXene was confirmed by the XRD pattern of the composite. The presence of a small signal at a 2θ value of 6.6° indicates that the MXene is incorporated successfully during the MOFMX composite formation, which is in line with the previously reported study.[26] The other XRD signal of the composite is similar to pristine MOF. However, a decrease in intensity and peak broadening was observed.[27]

The morphological aspects of the pristine Max phase, MXene, MOF and MOFMX composites were analyzed through field emission scanning electron micrographs (FESEM). Fig. S3a and b† show the pristine Max phase of $Mo_2Ti_2AlC_3$ 2D-layered material with large solid lumps. However, after etching "Al" with HF, prominent stacked 2D layered MXene ($Mo_2Ti_2C_3$) can be observed, as shown in Fig. S2b.† After etching and delamination, separated layers of the MXene are clearly observed in Fig. S3d.† (refs. [8] and 28) Fig. 2 shows the flower-like morphology of the pristine $CoNiNH_2BDC$ MOF with 2D flaked petals, similar to the previously reported layered 2D flake-like morphology.[26,29] $CoNiNH_2BDC$ MOF was grown on the surface of the layers of $Mo_2Ti_2C_3$ MXene. Fig. 2b clearly shows the growth of flaked $CoNiNH_2BDC$ MOF on the surface of delaminated 2D layers of MXene, which is also confirmed through the elemental mapping of the composite (Fig. 2c).

TEM analysis was also performed for MOFMX3 composites, and the images are depicted in Fig. 3, which shows a plate-like arrangement of MOF (light colored) on the surface of MXene.

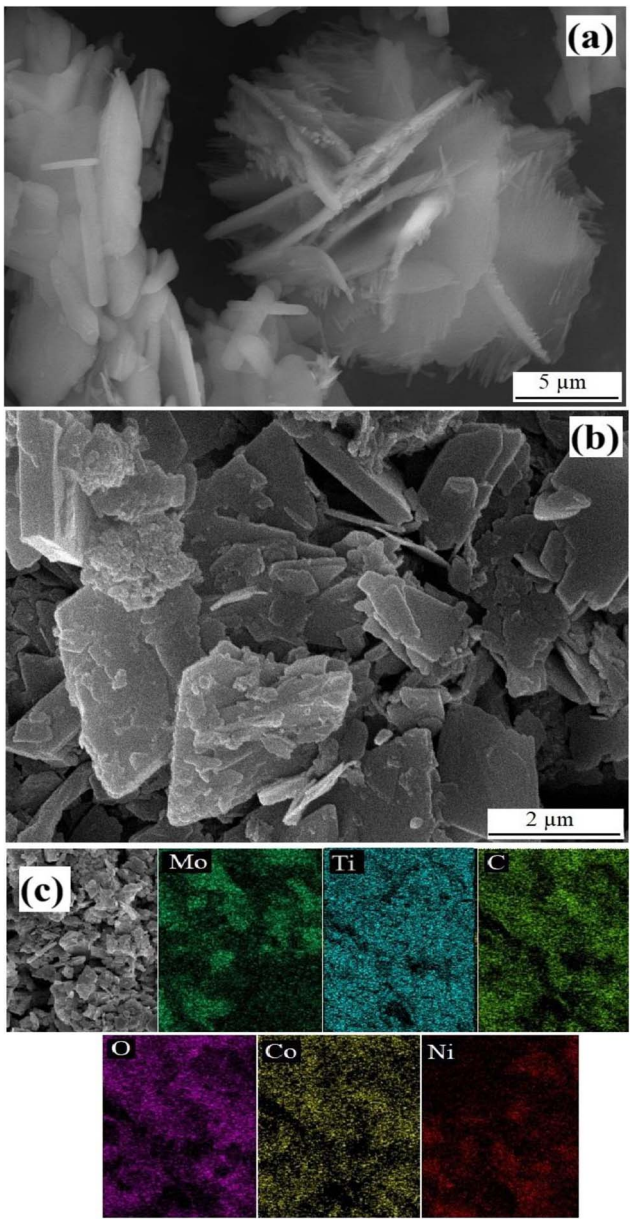

Fig. 2 FESEM of $CoNiNH_2BDC$ MOF (a), MOFMX3 composite (b) and elemental mapping (c).

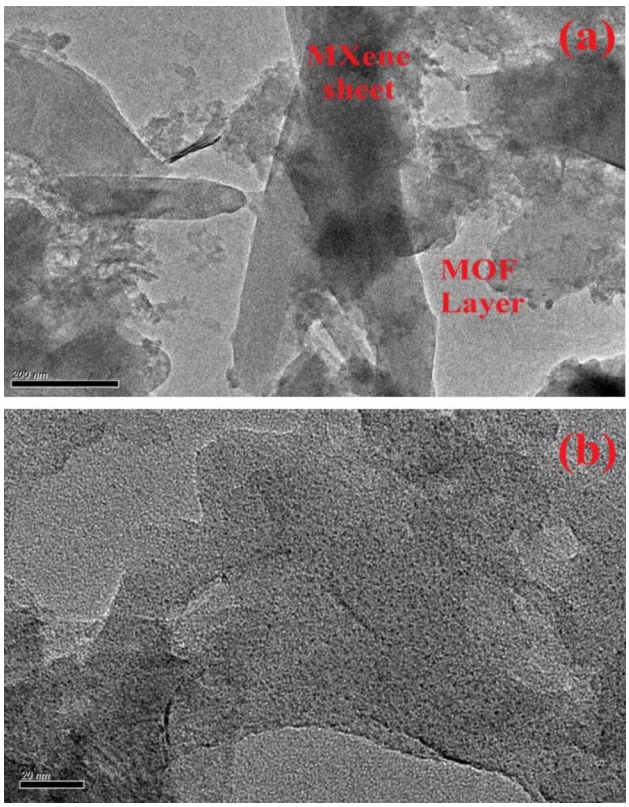

Fig. 3 TEM images of MOFMX3 composite (scale bar (a) 50 and (b) 20 nm).

The XPS survey scan of $Mo_2Ti_2C_3$ MXene, $CoNiNH_2BDC$ MOF, and MOFMX composites is shown in Fig. S4.† XPS survey scan of $Mo_2Ti_2C_3$ MXene shows the presence of Mo, Ti, C, O, and F, and the absence of Al confirms successful etching during MXene formation. The survey scan $CoNiNH_2BDC$ MOF shows the presence of Co, Ni, C, N, and O elements. The XPS of the MOFMX composite confirms the presence of all its elements from MOF and MXene, *i.e.*, Co, Ni, Mo, Ti, C, and O.

As shown in Fig. 4a, the high-resolution XPS spectra of Mo 3d in the MOFMX composite deconvoluted into three fitting crests at 228.8 eV, 232 eV and 235.3 eV, agreeing well with Mo–C ($3d_{5/2}$), Mo–C ($3d_{3/2}$), and Mo–Ox ($3d_{3/2}$) bonds, respectively.[13,23] Similarly, Fig. 4a (lower) shows the fine XPS spectra of Mo 3d of $Mo_2Ti_2C_3$ MXene where all the bands match well with the previously reported studies.[22,24] The XPS spectrum of Ti 2p (Fig. 4b) shows the binding energies at 454.8 eV and 460.6 eV,

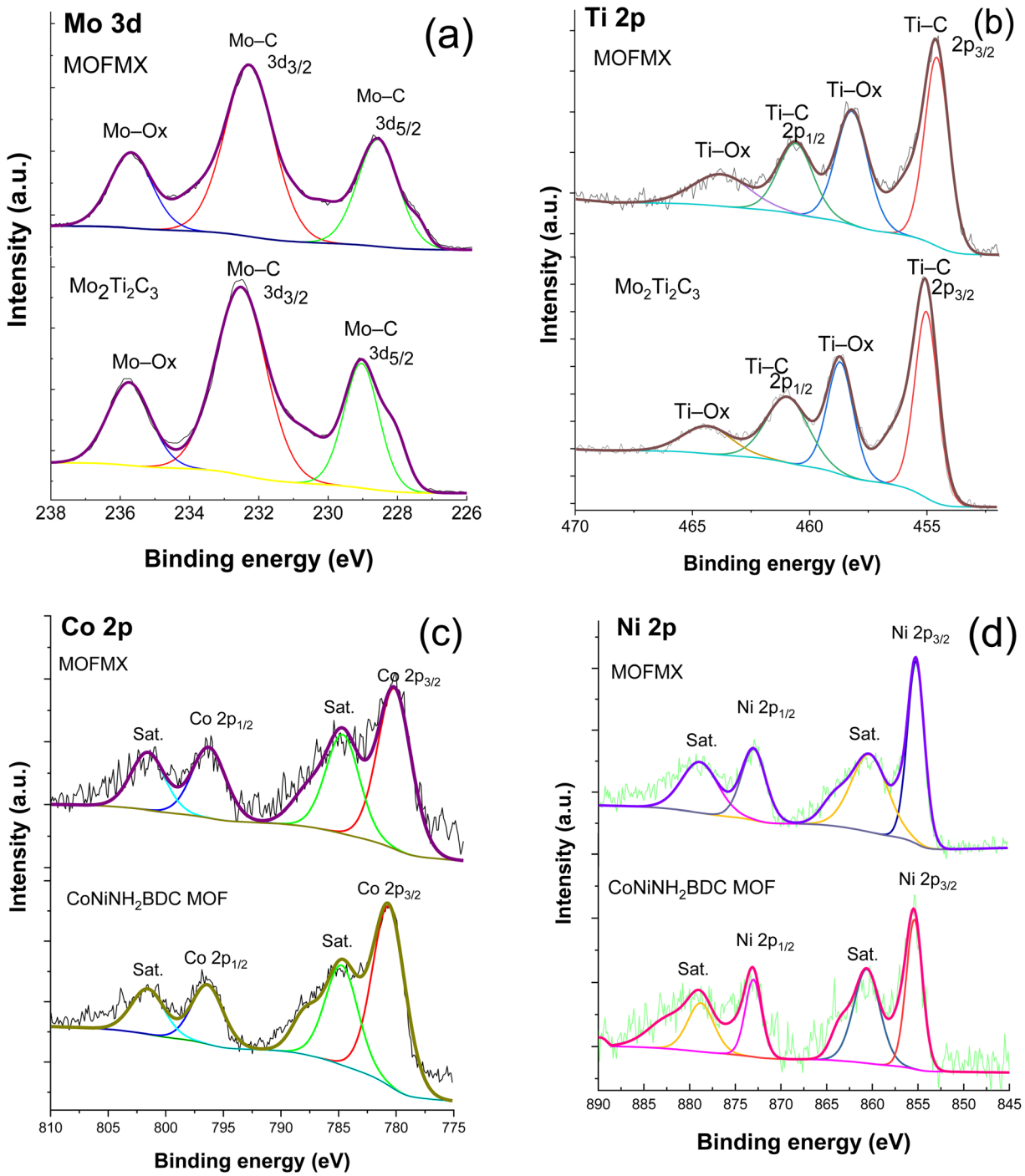

Fig. 4 High-resolution XPS of Mo 3d (a), Ti 2p (b), Co 2p (c), Ni 2p (d) of $CoNiNH_2BDC$, $Mo_2Ti_2C_3$ and MOFMX composite compared with each other.

the doublet allocated to Ti $2p_{3/2}$ and $2p_{1/2}$, respectively, which signifies Ti–C species, which agrees with the reported work.[30] Signals at 458.3 eV and 463.8 eV binding energies, respectively, demonstrate the oxidation states of Ti species (Ti–Ox, Ox = O, OH, F), as reported previously.[31] Similarly, within the Ti 2p spectrum Ti–Al entities were not present in both the XPS spectra of MOFMX composite and $Mo_2Ti_2C_3$ MXene, which indicates that Al was absent and MXene was etched properly; the Al layer was successfully removed by hydrofluoric acid (Fig. 4b lower). The presence of Mo 3d and Ti 2p in the MOFMX composite sample confirms the incorporation of MXene into the composite formation. The high-resolution spectra of Co 2p and Ni 2p of the MOFMX composite show the bands at binding energies of 780.8 eV ($2p_{3/2}$) and 796.4 eV ($2p_{1/2}$), and 855.1 eV ($2p_{3/2}$) and 872.4 ($2p_{1/2}$) eV, respectively, which are similar to the previously reported studies[25] (Fig. 4c and d). Additionally, two broad satellite peaks are observed in both of the cases Co 2p and Ni 2p at 784.8 eV and 801.6 eV, and 860.2 eV and 878.9 eV binding energies, respectively.[27,32] The carbon spectrum exhibits major bands (C 1s) at 284.77 eV, 285.9 eV, and 288.7 eV binding energies for the C–C bond, C–O and C=O species (Fig. S5†), respectively. Another broad peak at the binding energy of 282.4 eV was also observed, which confirms the presence of the C–M bond, similar to the C–M bond in $Mo_2Ti_2C_3$ MXene; however, this band is not observed in CoNiMOF, which suggests successful MOFMX composite formation (Fig. S5†). The XPS spectrum of O 1s shows the major deconvoluted peaks at binding energies of 531.2 eV and 532.6 eV and can be ascribed to O=C and O–C, respectively (Fig. S6†). The signal at the binding energy of 529.9 eV shows the existence of an O–M bond (M = Mo, Ti, Co, Ni), this signal is very prominent in the case of $Mo_2Ti_2C_3$ MXene (Fig. S6†). The presence of this signal further confirms the successful incorporation of MXene in the MOFMX composite, and it is backed by the reported studies.[26,31,33]

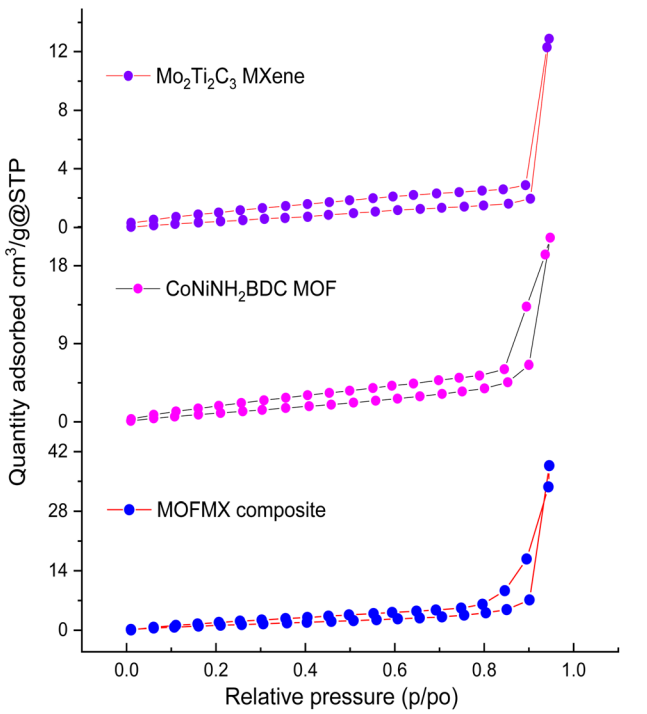

Fig. 5 N_2 adsorption/desorption isotherm of $Mo_2Ti_2C_3$ MXene, $CoNiNH_2BDC$ MOF and MOFMX3 composites.

To inquire about the specific surface area (S_{BET}) and porosity of $Mo_2Ti_2C_3$ MXene, $CoNiNH_2BDC$ MOF and MOFMX composite, nitrogen adsorption–desorption analysis was performed. The isotherm shape shows a type-IV curve with an H3 distinct hysteresis loop, which implies the existence of mesoporous pores.[29] $Mo_2Ti_2C_3$ MXene and $CoNiNH_2BDC$ MOF show the typical isotherm for layered structures with S_{BET} of 3.0 $m^2 g^{-1}$ and 11.2 $m^2 g^{-1}$, respectively. The enhanced surface area of the MOFMX composite was observed with the MXene addition and recorded as 14.6 $m^2 g^{-1}$ (Fig. 5), as in previously reported studies.[23,34] The increased surface area shows the growth and alignment of 2D MOF sheets with MXene nanosheets for the creation of void spaces of various sizes. The mesoporous structure of the MOFMX composite with a higher surface area is supposed to be accountable for improved electrocatalytic efficiency than pristine MOF, as discussed later in this work.

3.2. Electrocatalytic performance

The electrocatalytic efficiency of $NiNH_2BDC$, $CoNH_2BDC$, and $CoNiNH_2BDC$ was tested for both OER and HER using a three-electrode system in 0.1 M KOH solution (electrolyte). The electrocatalytic OER efficiency of the above-mentioned catalysts is shown by linear sweep voltammetry (LSV) (Fig. 6). From Fig. 6, we can conclude that bimetallic $CoNiNH_2BDC$ MOF showed enhanced OER activity compared to the pristine $CoNH_2BDC$ and $NiNH_2BDC$ MOFs, as it showed early onset potential and attained a current density of 10 mA cm^{-2} at 1.496 V *vs.* RHE. Equal loading of the catalyst on the conductive substrate was done, *i.e.*, 0.2 mg cm^{-2}. $Mo_2Ti_2C_3$ composites of $CoNiNH_2BDC$, MOFMX1, MOFMX2, and MOFMX3 were evaluated to measure the OER activity by LSV (Fig. 6a). MOFMX3 showed remarkable results with an early onset and obtained a 10 mA cm^{-2} current density at 1.443 V *vs.* RHE, while MOFMX1, MOFMX2, and MOFMX4 attained current densities of 10 mA cm^{-2} at 1.487 V, 1.453 V, and 1.451 V *vs.* RHE, respectively (Fig. 6 and S7†). MOFMX3 exhibits an exceptionally low overpotential of 215 mV, indicating efficient OER activity. MOFMX1 and MOFMX2 showed enhanced OER activity with overpotentials of 257 mV and 223 mV at 10 mA cm^{-2}, respectively, compared to $CoNiNH_2BDC$ with an overpotential value of 266 mV. As MXene is a conductive material, its layered structure increased the catalytic sites on the surface and hence enhanced OER performance from these hybrid materials; however, increasing the MXene concentration up to 15% (MOFMX3) is sufficient to have excellent OER activity (Fig S7†). Tafel slope values are shown in Fig. 6b, and MOFMX3 showed the lowest Tafel slope value of 44.8 mV dec^{-1}, while MOFMX1 showed 77 mV dec^{-1}, and MOFMX2 showed 57 mV dec^{-1}. However, $CoNiNH_2BDC$ possesses a higher Tafel slope value of 89 mV dec^{-1} among these catalysts. The lowest value of the Tafel slope for MOFMX3 indicates higher reaction kinetics. The remarkably good

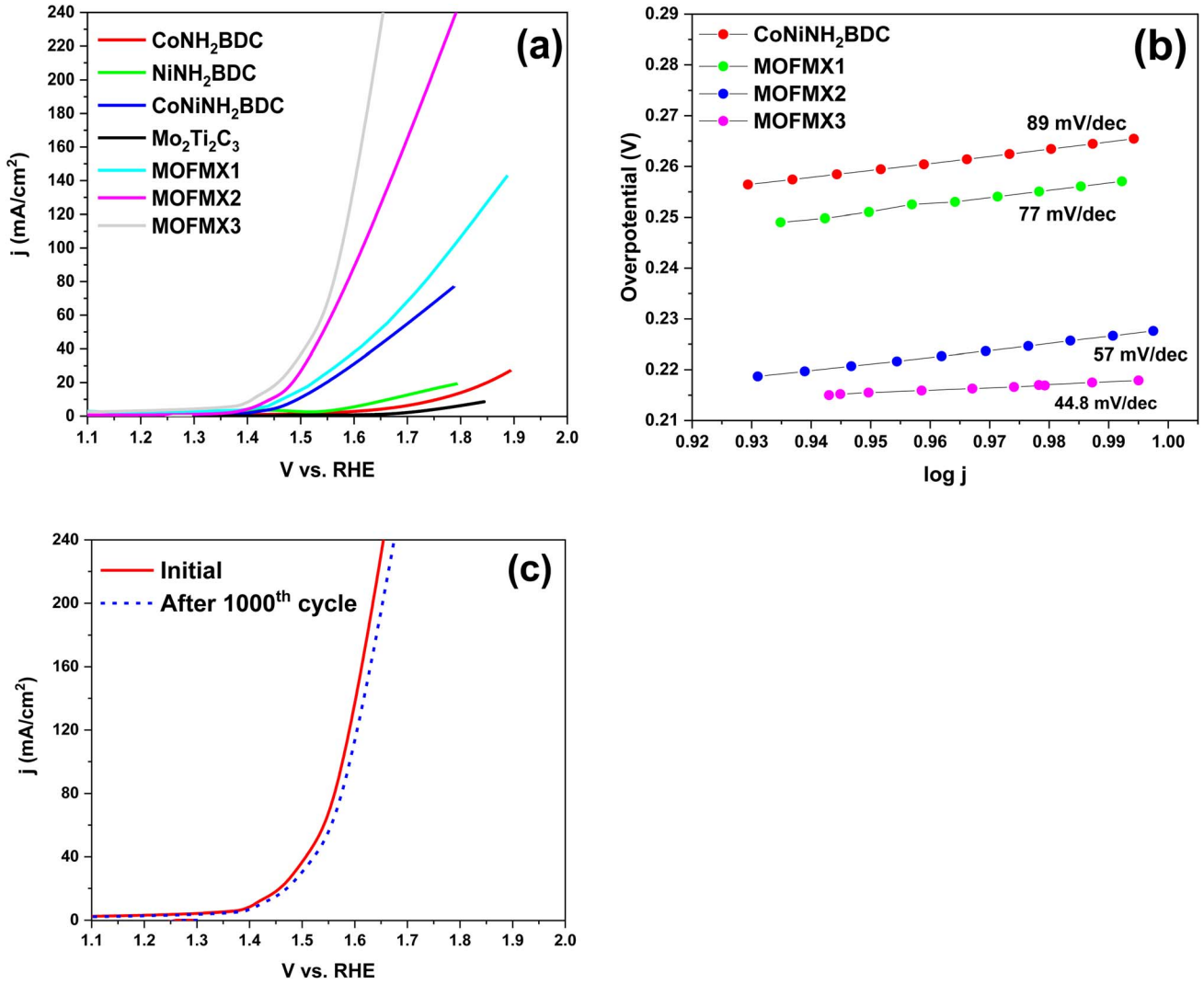

Fig. 6 Electrocatalytic OER efficiency (a) LSV curves, (b) Tafel slope, (c) LSV curves of MOFMX3 before and after 1000 CV cycles.

electrocatalytic OER performance of the $CoNiNH_2BDC$ MOF hybrid with $Mo_2Ti_2C_3T_x$ shows the synergistic effect of both components of this hybrid material. $CoNiNH_2BDC$ MOF has a porous structure and a large surface area and has shown good OER catalytic activity. A combination of $Mo_2Ti_2C_3T_x$ with $CoNiNH_2BDC$ MOF further increased the surface area, as shown in Fig. 5. Structural support is provided by MXene nanosheets to the MOF structure and enhances the exposed surface area; hence, the number of active sites increases, and MXene also helps in preventing the aggregation of layers and, therefore, enhanced surface area, which ultimately results in enhanced catalytic activity. Double layer capacitance (C_{dl}) at the liquid interface was measured by taking cyclic voltammetry (CV) at different scan rates of 50, 100, 150, 200, 250, and 300 mV s^{-1} in the non-faradaic region; j_{anodic}–$j_{cathodic}$/2 was plotted against scan rates, and C_{dl} was calculated from it. MOFMX3 showed the highest value of C_{dl} 9.42 mF cm^{-2} compared to the bare MXene (1.13 mF cm^{-2}), $CoNiNH_2BDC$ MOF (1.17 mF cm^{-2}), MOFMX1 (2.31 mF cm^{-2}), and MOFMX2 (7.52 mF cm^{-2}) (Fig. S8†). This clearly indicated that this hybrid did not only support the porous structure but also that there was easy access of the electrolyte to the catalytic active sites. Electrochemical impedance spectroscopy (EIS) measurement was done in the frequency ranging from 1 Hz to 1 kHz, and the Nyquist plot (Fig. S9†) of MXene and MOF showed higher charger transfer resistance in comparison to the MOFMX3 that showed the smallest semi-circle, indicating lowest charge transfer resistance, which is again confirmation of intrinsically high surface area, enhanced conductivity, and easy transfer of charges at the electrode–electrolyte interface. The stability of the catalyst was examined by continuous 1000 CVs at 5 mV s^{-1}, and it was observed that the initial and after CV cycles were majorly similar, indicating that this material was highly stable (Fig. 6c) .

The LSV curves of the as-prepared catalyst for HER activities are shown in Fig. 7a. It is evident from these LSVs that bimetallic $CoNiNH_2BDC$ showed the best HER results among the

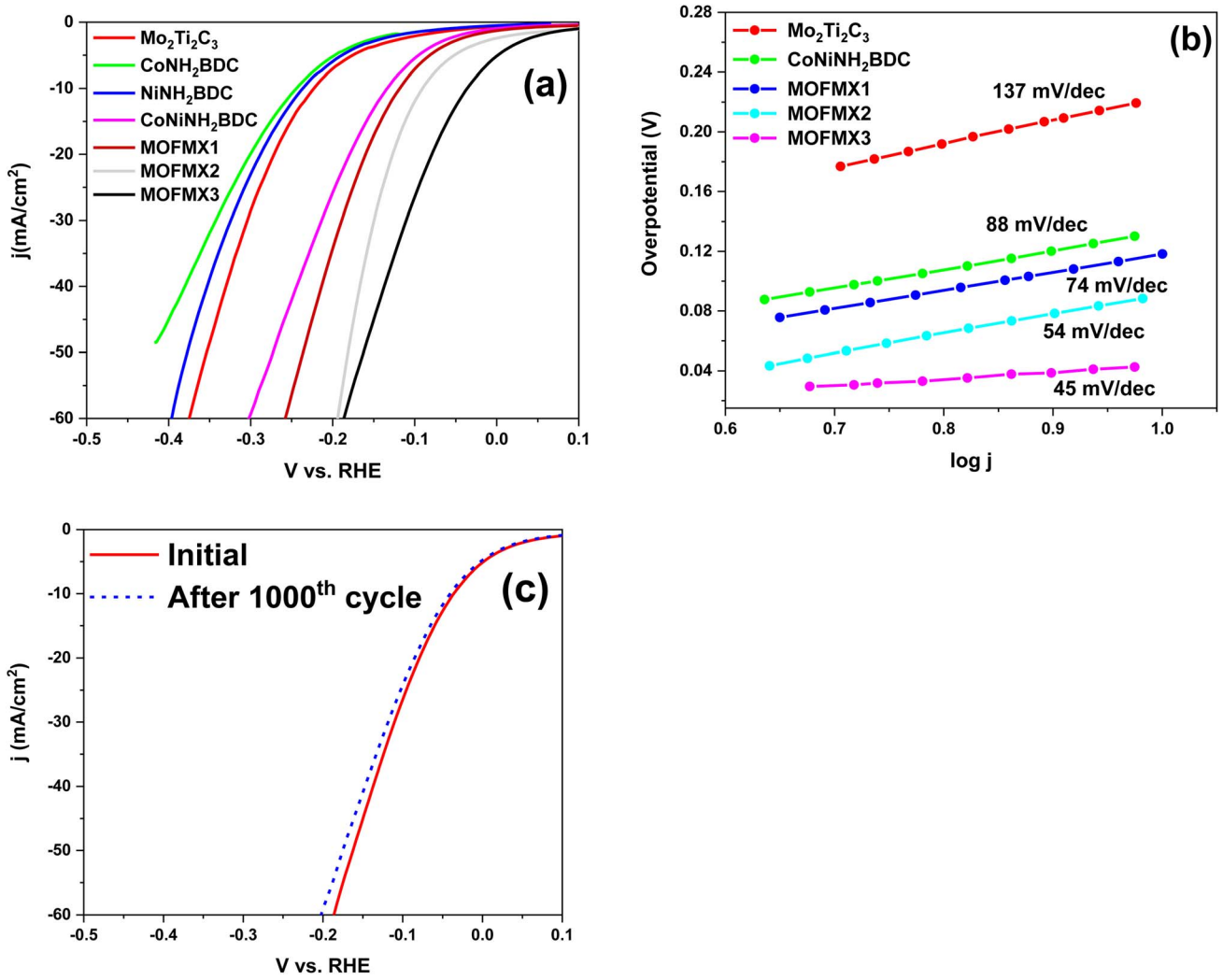

Fig. 7 Electrocatalytic HER efficiency (a) LSV curves, (b) Tafel slope, and (c) LSV curves of MOFMX3 before and after 1000 CV cycles.

above-mentioned catalysts, even though they were lower than those of MOFMX3. LSV curves of MOFMX1, MOFMX2, MOFMX3 and MOFMX4 composites are shown in Fig. S10.† It is evident that the HER activity shows an increasing trend by increasing MXene concentration in MOFMX composite and is maximum with MOFMX3, which is because the addition of MXene can facilitate electron transfer. However, beyond the optimum concentration of MXene, further addition can also block the catalytic active sites of the catalyst, thereby reducing the catalytic performance. Among the catalysts, MOFMX1, MOFMX2, and MOFMX3 achieved a current density of 10 mA cm^{-2} at 123 mV, 93 mV, and 37 mV, respectively, for HER, while $Mo_2Ti_2C_3T_x$ and $CoNiNH_2BDC$ MOF attained a current density of 10 mA cm^{-2} at 224 mV and 135 mV, respectively. MOFMX3 showed the earliest onset and lower overpotential value among these catalysts and hence the best HER performance among these. The Tafel slope value of MOFMX3 is smaller, and it indicates faster reaction kinetics of the catalyst towards HER (Fig. 7b). This could be possibly due to the formation of hydronium ions on the surface of the catalyst in 0.1 M KOH alkaline solution (electrolyte) and hence better catalytic activity and faster reaction kinetics as well. To inquire about the catalyst stability, continuous 1000 CVs were analyzed, and no significant difference in the initial LSV and after CV cycles LSV was observed, indicating that this material is highly stable (Fig. 7c).

Chronoamperometry measurement was also performed to examine the stability of the catalyst and was carried out at 1.48 V *vs.* RHE for OER and −0.04 *vs.* RHE for HER for 20 hours. Strong durability in a prolonged chronoamperometry test was shown by MOFMX3, and it exhibited slight degradation, demonstrating its high durability (Fig. 8). With uninterrupted measurements, 97% of the initial current density was retained for up to three hours, and 91% current density was retained up to 12 hours, which remained consistent for up to 20 h, demonstrating superb stability for OER. The stability test conducted for HER shows very little degradation of the current up to the first 8 h (99% efficiency). However, the degradation of current density after 8 h was observed, retained further until the

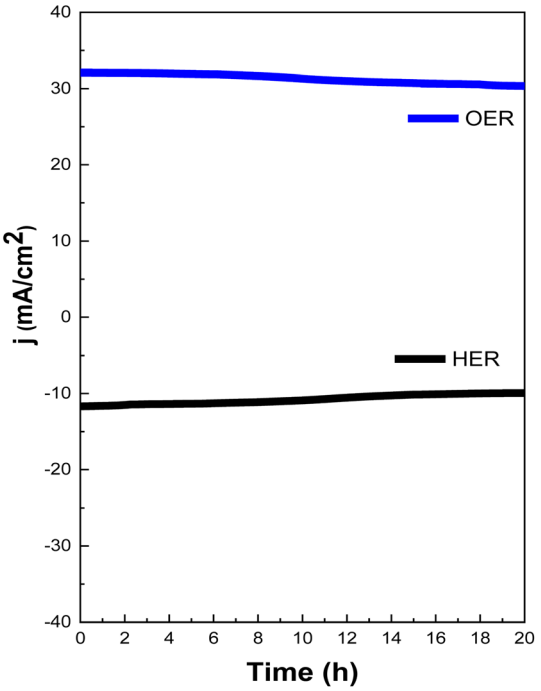

Fig. 8 Chronoamperometry-stability test of MOFMX3 for (a) OER and (b) HER.

maximum test period of 20 h and was able to maintain the efficiency of 97%. The lower stability of OER than HER may be due to the oxidation of MXene in an oxic environment, which results in a decrease in the active site.

Hence, the above-mentioned parameters have shown that combining MXene with MOF has proved that this hybrid is beneficial for enhancing the electrocatalytic performance of MOFs for both OER and HER. Interface engineering between catalysts through electronic metal support interaction has been proposed; it is in agreement with the effect of stabilization, and it is known that during the catalytic process of metal-based catalysts, reconstruction of the surface is observed.[35] In comparison to the pristine MOF, the prepared hybrid MOFMX3 offers a stable configuration, and the possible reason behind such high stability is the 2D structure of MXene that contributes to the enhancement of specific surface area, reduction in charge transfer resistance, and enhancement in the conductivity and contact area with electrolyte for efficient electrocatalysis.

Furthermore, an efficient role in this work was played by the strategy of the interdiffusion reaction for *in situ* growth of $CoNiNH_2BDC@Mo_2Ti2C3$ MXene, which resulted in faster charge transfer kinetics, enhanced conductivity, and hence upgraded bifunctional electroactivities for HER and OER. Table 1 shows a comparison of the current research with the previously reported studies. Metals such as Ni, Co, Fe, and Mo were the most studied elements for OER and HER activities and were used in various ways. For example, trimetallic NiCoFe-MOF-derived hollow nanocuboidals were reported as a dual catalyst in alkaline media and showed an overpotential of 320 mV for OER and 270 mV for HER at 10 mA cm^{-2} This study shows that the heteroatom doping tuned the electronic structure, resulting in electroactivities toward OER and HER.[36] Single and bimetallic pristine MOFs and MOFs supported on conductive materials were also reported for enhanced electroactivities toward OER and HER.[19,37,38] Similarly, pristine Mo_2CT_x MXene and MXene hybrids with Co, CoP and Co–MoS_2 are also reported;[39–41] however, their HER electroactivities are far lower than the currently reported bifunctional catalyst MOFMX.

Table 1 Comparison table for OER and HER activities at a current density of 10 mA cm^{-2}

Catalyst	Reaction	Electrolyte	Overpotential (mV) at 10 mA cm^{-2}	Tafel slope (mV dec^{-1})	Substrate	Ref.
NiCoFe-MOF-derived hollow multivoid nanocuboidal catalyst	OER	0.1 M KOH	320	49	GCE	36
CoP@3D Ti_3C_2-MXene	OER	1.0 M KOH	290	51	GCE	40
2D Co-BDCMOF nanosheets	OER	1 M KOH	263	74	GCE	37
Fe/Ni-BTC@NF	OER	0.1 M KOH	270	—	NF	19
$Ti_3C_2T_x$-Co/Ni-BDC	OER	1 M KOH	265	51.7	CP	25
2D Ni-MOF@Fe-MOF nanosheets	OER	1 M KOH	265	82	GCE	38
$FeNiNH_2BDC$@5 wt% CNTs	OER	1 M KOH	220	68.5	GCE	42
Fe/Ni-MOF	OER	1 M KOH	236	49	NF	43
$Fe_xNi_{1-x}(OH)_2$	OER	1 M NaOH	311	—	GCE	44
MOFMX3 ($CoNiNH_2BDC@Mo_2Ti_2C_3$)	OER	0.1 M KOH	215	44.8	GCE	This work
CoP@3D Ti_3C_2-MXene	HER	1.0 M KOH	168	58	GCE	40
NiCoFe-MOF derived hollow multivoid nanocuboidal catalyst	HER	0.1 M KOH	270	—	GCE	36
Mo_2CTx : Co (single site Co substitution)	HER	0.5 M H_2SO_4	180	59	GCE	39
Ni_2P–$Ni_{12}P_5$@Ni_3S_2/NF	HER	0.5 M H_2SO_4	46	78	NF	45
Co–MoS_2/Mo_2CT_x	HER	1.0 M KOH	112	82	GCE	41
$CoSe_2$/CoP	HER	1 M KOH	65	54	GCE	46
MoO_2/MoS_2/C	HER	1 M KOH	91	49	NF	47
Mo_2CT_x MXene	HER	0.5 M H_2SO_4	283	82	GCE	24
MOFMX3 ($CoNiNH_2BDC@Mo_2Ti_2C_3$)	HER	0.1 M KOH	37	45	GCE	This work

Conclusion

This work presented the use of a bimetallic 2D MOF grown on the surface of a 2D bimetallic MXene using an interdiffusion synthesis strategy. The negatively charged $Mo_2Ti_2C_3$ was tightly bound to the positively charged $CoNiNH_2BDC$, and the strong interface between the two components of the hybrid resulted in rapid charge transfer for enhanced electrocatalytic activity. Both FESEM and TEM supported the stacking of 2D MOF on the surface of the delaminated sheets of MXene. The most efficient catalyst among the catalysts investigated in this work is MOFMX3, and it showed the lowest overpotential value of 215 mV for OER and 37 mV for HER, the lowest Tafel slope of 44.8 mV dec^{-1} for OER and 45 mV dec^{-1} for HER and a higher C_{dl} value of 9.42 mF cm^{-2}. These values indicate that the catalyst's performance was equivalent to, or even better than the reported transition metal-based electrocatalysts. Overall, this work showed the synergistic effect of combining MXene and MOFs as this combination provides support to the structure and enhances the exposed surface area and hence the number of active sites increases. MXene also helps in preventing the aggregation of MOF layers and therefore enhances surface area, which ultimately results in enhanced catalytic activity towards OER and HER under alkaline conditions. Considering the structural properties of both MOF and MXene materials and their synergistic effects, this work supports the idea of introducing more multifunctionality to the MOFs by combining them with conducting materials for enhanced electrochemical water splitting for clean hydrogen production.

Data availability

The data supporting this article have been included as part of the ESI.†

Conflicts of interest

There are no conflicts to declare.

Acknowledgements

We greatly appreciate the financial assistance of Pakistan Science Foundation under project no. PSFNSFC-IV/Chem/C-QAU (27).

References

1 S. Chu and A. Majumdar, *nature*, 2012, **488**(7411), 294–303.
2 S. E. Hosseini and M. A. Wahid, *Renewable Sustainable Energy Rev.*, 2016, **57**, 850–866.
3 Z. Xia, *Nat. Energy*, 2016, **1**(10), 1–2.
4 A. Bavykina, N. Kolobov, I. S. Khan, J. A. Bau, A. Ramirez and J. Gascon, *Chem. Rev.*, 2020, **120**(16), 8468–8535.
5 Y. Pan, J. Wang, S. Chen, W. Yang, C. Ding, A. Waseem and H.-L. Jiang, *Chem. Sci.*, 2022, **13**(22), 6696–6703.
6 S. S. A. Shah, T. Najam, M. Wen, S.-Q. Zang, A. Waseem and H.-L. Jiang, *Small Struct.*, 2022, **3**(5), 2100090.
7 Y. Xu, Q. Li, H. Xue and H. Pang, *Coord. Chem. Rev.*, 2018, **376**, 292–318.
8 S. Kashif, S. Akram, M. Murtaza, A. Amjad, S. S. A. Shah and A. Waseem, *Diamond Relat. Mater.*, 2023, **136**, 110023.
9 S. S. A. Shah, M. Sohail, G. Murtza, A. Waseem, A. U. Rehman, I. Hussain, M. S. Bashir, S. S. Alarfaji, A. M. Hassan, M. A. Nazir, M. S. Javed and T. Najam, *Chemosphere*, 2024, **349**, 140729.
10 D. Senthil Raja, X. F. Chuah and S. Y. Lu, *Adv. Electron. Mater.*, 2018, **8**(23), 1801065.
11 S. Wang, Z. Ai, X. Niu, W. Yang, R. Kang, Z. Lin, A. Waseem, L. Jiao and H.-L. Jiang, *Adv. Mater.*, 2023, **35**(39), 2302512.
12 M. Khazaei, M. Arai, T. Sasaki, A. Ranjbar, Y. Liang and S. Yunoki, *Phys. Rev. B*, 2015, **92**(7), 075411.
13 M. Saraf, B. Chacon, S. Ippolito, R. W. Lord, M. Anayee, R. Wang, A. Inman, C. E. Shuck and Y. Gogotsi, *Adv. Funct. Mater.*, 2024, **34**(1), 2306815.
14 T. Xu, Y. Wang, Y. Xue, J. Li and Y. Wang, *Chem. Eng. J.*, 2023, **470**, 144247.
15 M. Murtaza, K. Farooq, A. A. Amjad, S. S. A. Shah and A. Waseem, *Diamond Relat. Mater.*, 2024, **147**, 111379.
16 S. Gopi, A. Panda, A. Ramu, J. Theerthagiri, H. Kim and K. Yun, *Int. J. Hydrogen Energy*, 2022, **47**(100), 42122–42135.
17 A. Zhang, R. Liu, J. Tian, W. Huang and J. Liu, *Chem.–Eur. J.*, 2020, **26**(29), 6342–6359.
18 Z. Xue, K. Liu, Q. Liu, Y. Li, M. Li, C. Y. Su, N. Ogiwara, H. Kobayashi, H. Kitagawa, M. Liu and G. Li, *Nat. Commun.*, 2019, **10**(1), 5048.
19 L. Wang, Y. Wu, R. Cao, L. Ren, M. Chen, X. Feng, J. Zhou and B. Wang, *ACS Appl. Mater. Interfaces*, 2016, **8**(26), 16736–16743.
20 L. Zhao, B. Dong, S. Li, L. Zhou, L. Lai, Z. Wang, S. Zhao, M. Han, K. Gao and M. Lu, *ACS Nano*, 2017, **11**(6), 5800–5807.
21 M. Ali, E. Pervaiz and O. Rabi, *ACS Omega*, 2021, **6**(50), 34219–34228.
22 F. Hu, X. Wang, H. Niu, S. Zhang, B. Fan and R. Zhang, *J. Mater. Sci.*, 2022, **57**(16), 7849–7862.
23 L. Ding, Y. Tang, S. Wang, Y. Zhang, X. Chen and H. Zhou, *J. Colloid Interface Sci.*, 2024, **653**, 1671–1682.
24 Z. W. Seh, K. D. Fredrickson, B. Anasori, J. Kibsgaard, A. L. Strickler, M. R. Lukatskaya, Y. Gogotsi, T. F. Jaramillo and A. Vojvodic, *ACS Energy Lett.*, 2016, **1**(3), 589–594.
25 P. Tan, R. Gao, Y. Zhang, N. Han, Y. Jiang, M. Xu, S.-J. Bao and X. Zhang, *J. Colloid Interface Sci.*, 2023, **630**, 363–371.
26 L. Wang, L. Song, Z. Yang, Y.-M. Chang, F. Hu, L. Li, L. Li, H.-Y. Chen and S. Peng, *Adv. Funct. Mater.*, 2023, **33**(1), 2210322.
27 Y. Wen, Z. Wei, C. Ma, X. Xing, Z. Li and D. Luo, *Nanomaterials*, 2019, **9**(5), 775.
28 K. Farooq, M. Murtaza, Z. Yang, A. Waseem, Y. Zhu and Y. Xia, *Nanoscale Adv.*, 2024, **6**, 3169–3180.
29 S. Y. Lee, H. J. An, J. Moon, D. H. Kim, K. W. Park and J. T. Park, *Electrochim. Acta*, 2023, **451**, 142291.
30 A. Lipatov, M. Alhabeb, M. R. Lukatskaya, A. Boson, Y. Gogotsi and A. Sinitskii, *Adv. Electron. Mater.*, 2016, **2**(12), 1600255.

31 J. Halim, K. M. Cook, M. Naguib, P. Eklund, Y. Gogotsi, J. Rosen and M. W. Barsoum, *Appl. Surf. Sci.*, 2016, **362**, 406–417.
32 P. Thangasamy, S. Shanmuganathan and V. Subramanian, *Nanoscale Adv.*, 2020, **2**(5), 2073–2079.
33 G. Li, B. Zhou, P. Wang, M. He, Z. Fang, X. Yuan, W. Wang, X. Sun and Z. Li, *Angew. Chem., Int. Ed.*, 2022, **12**(8), 850.
34 R. Ramachandran, K. Rajavel, W. Xuan, D. Lin and F. Wang, *Ceram. Int.*, 2018, **44**(12), 14425–14431.
35 F.-Y. Chen, Z.-Y. Wu, Z. Adler and H. Wang, *Joule*, 2021, **5**(7), 1704–1731.
36 W. Ahn, M. G. Park, D. U. Lee, M. H. Seo, G. Jiang, Z. P. Cano, F. M. Hassan and Z. Chen, *Adv. Funct. Mater.*, 2018, **28**(28), 1802129.
37 Y. Xu, B. Li, S. Zheng, P. Wu, J. Zhan, H. Xue, Q. Xu and H. Pang, *J. Mater. Chem. A*, 2018, **6**(44), 22070–22076.
38 K. Rui, G. Zhao, Y. Chen, Y. Lin, Q. Zhou, J. Chen, J. Zhu, W. Sun, W. Huang and S. X. Dou, *Adv. Funct. Mater.*, 2018, **28**(26), 1801554.
39 D. A. Kuznetsov, Z. Chen, P. V. Kumar, A. Tsoukalou, A. Kierzkowska, P. M. Abdala, O. V. Safonova, A. Fedorov and C. R. Müller, *J. Am. Chem. Soc.*, 2019, **141**(44), 17809–17816.
40 L. Xiu, Z. Wang, M. Yu, X. Wu and J. Qiu, *ACS Nano*, 2018, **12**(8), 8017–8028.
41 J. Liang, C. Ding, J. Liu, T. Chen, W. Peng, Y. Li, F. Zhang and X. Fan, *Nanoscale*, 2019, **11**(22), 10992–11000.
42 L. Yaqoob, T. Noor, N. Iqbal, H. Nasir, N. Zaman and K. Talha, *J. Alloys Compd.*, 2021, **850**, 156583.
43 F. Zheng, Z. Zhang, D. Xiang, P. Li, C. Du, Z. Zhuang, X. Li and W. Chen, *J. Colloid Interface Sci.*, 2019, **555**, 541–547.
44 S. L. Candelaria, N. M. Bedford, T. J. Woehl, N. S. Rentz, A. R. Showalter, S. Pylypenko, B. A. Bunker, S. Lee, B. Reinhart and Y. Ren, *ACS Catal.*, 2017, **7**(1), 365–379.
45 H. Yang, P. Guo, R. Wang, Z. Chen, H. Xu, H. Pan, D. Sun, F. Fang and R. Wu, *Adv. Mater.*, 2022, **34**(20), 2107548.
46 S. Shen, Z. Wang, Z. Lin, K. Song, Q. Zhang, F. Meng, L. Gu and W. Zhong, *Adv. Mater.*, 2022, **34**(13), 2110631.
47 F. Gong, M. Liu, S. Ye, L. Gong, G. Zeng, L. Xu, X. Zhang, Y. Zhang, L. Zhou and S. Fang, *Adv. Funct. Mater.*, 2021, **31**(27), 2101715.